Flowfield Simulation About the Stratospheric Observatory for Infrared Astronomy

Christopher A. Atwood* and William R. Van Dalsem†

NASA Ames Research Center, Moffett Field, California 94035

The Reynolds-averaged Navier-Stokes equations have been applied to stratospheric observatory for infrared astronomy (SOFIA) configurations. Comparisons between numerical and experimental results are made in two dimensions for free shear layers and a rectangular cavity, and in three dimensions for simplified SOFIA geometries. Dominant acoustic behavior of the cavity flows compare well with experiment. The sensitivity of the solutions to changes in grid cell size and artificial dissipation levels are shown. Furthermore, optical path distortion due to the flowfield is modeled using geometrical constructs. The results demonstrate the viability and usefulness of the present computational method for this class of unsteady applications.

Nomenclature

a, b, c, d, e	=	position vectors
c	=	speed of sound
D, L, W	=	cavity depth, length, or width
f	=	frequency
K	=	ratio of vortex to freestream speeds
M	=	Mach number
n	=	absolute index of refraction
$\mathbf{n}$	=	surface normal
OPD, OPL	=	optical path difference or length
PSD	=	power spectral density
p	=	static pressure
Q	=	vector of dependent variables
Re	=	Reynolds number
SPL	=	sound pressure level
t	=	time or parametric ray coordinate
$\mathbf{t}$	=	tangential direction
u, v, w	=	Cartesian velocity components or parametric surface coordinates
α	=	angle of attack
β	=	Gladstone-Dale constant, $n - 1$
θ	=	angle subtending the ray and normal
λ	=	wavelength
ν	=	Courant-Friedrichs-Lewy number
ρ	=	density
σ	=	measure of shear layer spread rate

Subscripts

i, n, r	=	incident, normal, or refracted
rms	=	root-mean-square quantity
STP	=	standard temperature and pressure
T	=	stagnation quantity
∞	=	freestream quantity

Introduction

T HE SOFIA will be a 3-m class Cassegrain telescope which utilizes a Boeing 747SP as an observation platform. This project, shown conceptually in Fig. 1, is currently a cooperative effort between the U.S.'s NASA and Germany's DARA. Airborne observation systems of this type offer capabilities which augment land- and space-based options. First, the mission flexibility of a long-range mobile platform lends astronomers freedom to investigate transient astronomical phenomena on a global basis. Second, atmospheric attenuation of some wavelengths of interest provide motivation for a platform which operates above the tropopause. Third, the cost of maintaining and upgrading observation technologies is lower than would be incurred with an orbiting configuration.

Nevertheless, the use of an aircraft-based observatory presents some challenges. The limited bandwidth of solid materials in the infrared frequency ranges of interest preclude their use as a window. Therefore, the telescope cavity must remain open to the freestream. Wind-tunnel tests have shown that violent shear layer oscillations with concomitantly dangerous levels of acoustic loading occur for rectangularly shaped, or untreated, open cavity configurations.[1] Therefore, there is a need to develop cavity flow control treatments to suppress the flow unsteadiness. Risk of injury to the crew or damage to the platform is being reduced through the use of both experimental and computational fluid dynamics (EFD and CFD) analyses in the design phase. The objective of this effort is the development of CFD tools to be used in the SOFIA design and operational phases.

The driven cavity problem has been a subject of much experimental research[2,3] and numerical simulation of this class of problems has also been investigated by many researchers.[4-11] Komerath et al.[12] provided a review of open cavity research conducted during the past four decades. The present work builds on past numerical studies by first validating the ability to predict shear layer and generic cavity flowfields,[2] including detailed numerical sensitivity studies, and then applying the code to both untreated and treated cavity SOFIA configurations. The treated cavity SOFIA computation includes a model of the telescope as well as the aperture shape modifications. By comparing computed SOFIA flowfields to available experimental data,[1] we assess the capability to pre-
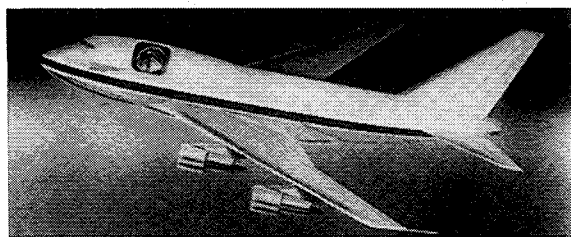
*Research Scientist, MCAT Institute. Member AIAA.
†Research Scientist and Group Leader. Member AIAA.

Fig. 1 Artist's concept of the SOFIA configuration.

dict the characteristics of the untreated SOFIA configuration and also one of the proposed flow control designs. Accurate prediction of the acoustic intensity levels and frequencies are of particular interest. If successful, this should develop the confidence required to use the developed CFD model in future SOFIA design studies. In addition to the unsteady flow results, efforts toward prediction of image distortion caused by the flow density variations are also presented.

The following sections address the method used to predict the unsteady flows, including the modeling of turbulence and the optical distortion. Results are presented for several two-dimensional cases and for two three-dimensional SOFIA configurations.

Numerical Methods

The objective of the numerical simulation of the flow about the SOFIA airborne observatory is to design a safe configuration which will have the least detrimental effects upon the optics. Towards this goal, the following transonic cavity flow problems were divided into three sections. First, the unsteady interaction of the external flow with the cavity requires time-dependent solutions to the Reynolds-averaged Navier-Stokes equations. Second, the shear layer growth rate is strongly dependent on turbulence effects which must be modeled due to the grid coarseness. Third, the optical model is applied to the unsteady density field to provide a measure of image distortion. Following discussion of the above models, boundary treatment and grid generation methods are presented.

Navier-Stokes Model

The algorithms used for this effort, coded by Buning and Chan,[13] are implemented within the Chimera overset grid framework.[14] The solutions were obtained using a diagonal scheme,[15] using spatially varying time steps for steady state computations, and fixed step size for unsteady flow simulations. The code utilizes a dependent variable vector of the form $Q = [\rho, \rho u, \rho v, \rho w, e]^T$ and pseudo-finite-volume metrics. Euler implicit time marching and second-order spatial differencing was used for the computations presented here. Computations were performed on the numerical aerodynamic simulator (NAS) Cray Y-MP/832 using the solid-state storage device, at an expense of 14 μs/point/iteration.

Turbulence Model

Turbulence is modeled using the method of Baldwin and Lomax[16] modified with a variable F_{max} cutoff and a shear layer model. Viscous walls were specified such that the search for F_{max} terminated before leaving the boundary-layer region. The eddy viscosity in the shear layer was computed as outlined by Buning.[13] However, for this effort σ_0 was set to 11.0 according to established experimental values.[17] It should be noted that previous numerical investigations indicate that the capture of cavity resonance is not strongly dependent upon the turbulence model in the cavity.[4,8,9]

Geometric Optics

The variation of the speed of light through gases is primarily a function of the density field. This fact has been extensively used to benefit the study of fluid physics, as exemplified by use of schlieren, shadowgraph, and interferometry techniques. The objective of this effort is to predict the distortion of an image caused by variations in the air density within the shear layer. Distortion is computed by using the density field history within the shear layer to predict variations in the optical path length using geometric optics. This will in turn allow prediction of the minimum resolvable astronomical feature, and contribute to the telescope design specifications.

The geometric optics model developed here assumes that the impact of the fluid density on the optical field may be computed by casting light rays through a discretized field. The simplifications afforded by the use of planar facets and piecewise continuous media are utilized by tesselation of each hex-
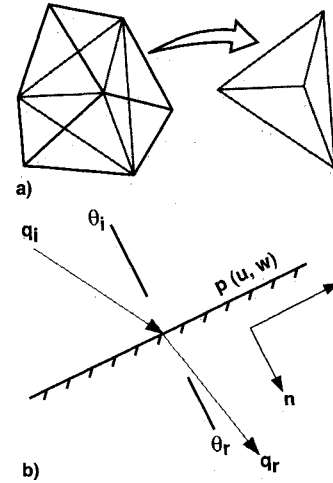

Fig. 2 a) Tesselation and b) intersection and refraction procedure.

ahedron of the flowfield domain into five tetrahedrons as shown in Fig. 2.

The problem can now be divided into three steps: 1) propagation of the ray, 2) intersection of the ray with a facet, and 3) refraction. Solution for the point contained in both the facet p and the ray q_i results in the intersection in parametric coordinates:

$$q_i(t) = d + et; \qquad p(u, w) = a + bu + cw$$

$$(b \times c) \cdot p = (b \times c) \cdot q_i$$

$$t = \frac{(b \times c) \cdot a - (b \times c) \cdot d}{(b \times c) \cdot e}$$

$$u = \frac{(c \times e) \cdot d - (c \times e) \cdot a}{(c \times e) \cdot b}$$

$$w = \frac{(b \times e) \cdot d - (b \times e) \cdot a}{(b \times e) \cdot c}$$

Specification of the light ray origin and a direction initializes the problem. Following the search for the initial hexahedral cell in which the ray originates, the tetrahedron within this hexahedron must be computed. The shortest intersection distance of the ray with the 16 facets which compose the hexahedron determines the origin tetrahedron. Subsequent intersection and refraction processes are a marching procedure. The OPL is found from

$$\mathrm{OPL} = \int n(s) \, \mathrm{d}s \approx \sum_j n_j \Delta s_j$$

and variation of the OPL over the aperture gives a measure of the wavefront error caused by the shear layer.

The refraction process is determined according to Snell's law as shown in Fig. 2. Generalization to three dimensions is accomplished by rotation to the osculating plane, which includes the surface normal and both the incident and refracted rays. In this osculating plane, a rotated local coordinate system is defined

$$q_i = |q_{i_n}|\hat{n} + |q_{i_t}|\hat{t}$$

where

$$|q_{i_n}| = |q_i|\cos \theta_i$$

$$|q_{i_t}| = |q_i|\sin \theta_i$$

$$\hat{t} = \frac{\hat{q}_i - \hat{n} \cos \theta_i}{\sin \theta_i}$$

Application of Snell's law $n_i \sin \theta_i = n_r \sin \theta_r$, where $n = 1 + \beta(\rho/\rho_{STP})$ results in an expression for the refracted ray

$$\hat{q}_r = \hat{n} \cos \theta_r + \hat{t} \sin \theta_r$$

The local index of refraction n_j is found by arithmetically averaging the densities at the four vertices of the tetrahedron. β is a function of the media and of the wavelength. Using air as the media and a wavelength of $\lambda = \lambda_D = 5893$ Å, then $\beta = 2.92 \times 10^{-4}$. The wavelengths of interest for SOFIA range from the near infrared, 1 μm, to the microwave, 1 mm. However, optical distortion is more severe for shorter wavelengths, hence the choice of yellow sodium light, λ_D.

Finally, to obtain a measure of the loss in irradiance due to the fluctuating density field, the OPL for vacuum conditions is subtracted from the OPL through the gas to yield the optical path difference (OPD). The value of OPD$|_{rms}$ is computed using a sequence of OPD at a fixed station. Using the rms wavefront distortion (σ), the phase distortion (Φ) is found from $\Phi = (2\pi\sigma/\lambda)$. The Strehl ratio, given by $I/I_0 = e^{-\Phi^2}$, is a measure of the peak intensity to which a beam can be focused. The computational expense of the procedure outlined above is currently 250 μs/hexahedron/ray on the NAS Cray 2.

Boundary Conditions

The viscous impermeable wall conditions are no-slip, zero normal pressure gradient, and adiabatic. Information transfer across overset mesh boundaries is implemented using nonconservative trilinear interpolation of Q. Treatment of the farfield boundaries is case dependent and is noted in the results section.

Geometry Treatment

A discussion of the treatment of the surface, the grid topology, and the grid strategy is given below.

Surface Modeling

The geometry used for the SOFIA configurations utilized clipped wings to emulate the experiment, which in turn allowed a cavity of more realistic size to be studied. The fuselage, wing, fairing, nacelles, and telescope geometry were obtained from two CAD data bases, and positioning errors in these data bases were corrected using blueprints.

The acquisition of the quiet configuration (100) aperture grid warrants additional comment. Wind-tunnel testing resulted in a hand-formed ramp and aperture (see Fig. 15) which was subsequently laser digitized.[19] This data, accurate to approximately 0.2 mm, was then converted into a form suitable for the surface grid.[20]

Surface definition via bicubic surfaces in regions of high curvature can cause local oscillatory behavior.[18,20] Along overlapping surfaces this property is manifested as C^0, or jump discontinuities at overset zone boundaries. These discontinuities in the discretized surface are ameliorated through bilinear projection from one zone face to another.[22] Typically, the projection distance is five orders of magnitude smaller than a characteristic geometry length.

Topology

The overset grid topology scheme was chosen for its geometric flexibility and the relative ease in which grid refinement can be implemented on individual zones. The use of a different grid for each component of the geometry simplifies changes that will occur as the design matures. For example, the geometries with cavities were built upon the clean configuration grids, saving many man-hours. The topology in the cavity region was chosen to allow rapid evaluation of new configurations and permit simple specification of turbulent wall and shear layer regions.

Grids

The grids for these simulations were obtained by way of algebraic[21] and hyperbolic[23] means, the topology was chosen to allow the use of these grid generation methods. Generally a wall spacing of $y^+ = 4.0$ was estimated for the viscous walls, the farfield boundary was placed at 20 fuselage diameters, and the outflow 10 diameters downstream. Damping of acoustic waves at the farfield boundary was achieved by the use of large cells which were unable to support high frequency waves.

The clean configuration, without a cavity, was modeled using four grids for the half-body: 1) the fuselage, 2) wing, 3) wing tip, and 4) nacelle. The grid point count was approximately 4×10^5. The fuselage grid was refined in the cavity region to provide similarly sized cells in interpolation regions.

The untreated aperture geometry, configuration 25 of the wind-tunnel test, was discretized by reflection of the clean case grids and addition of two meshes for the asymmetric cavity. The fuselage zone boundaries were shifted meridionally to move interpolation away from the cavity region. The two additional grids consisted of an outer cavity grid surrounding the cavity region and an inner cavity grid which included the cavity walls and the shear layer region. The outer zone was utilized to isolate the cavity unsteadiness from the global solution. The total grid point count was about 1.2×10^6 distributed in 10 zones.

The treated aperture geometry, configuration 100 of the wind-tunnel test, was modeled by addition of seven grids to the clean case: isolation, aperture wall, shear layer, cavity wall, telescope tub, secondary mirror, and an inner ramp grid. The total grid point count was about 1.8×10^6 in 15 zones.

Results and Discussion

Validation of the code was accomplished by evaluation of two- and three-dimensional cases. Numerical results for free shear layer and rectangular two-dimensional cavity flows were compared with analytic and experimental data to evaluate fundamental physics capturing capabilities. Analysis of the SOFIA configuration simulations, including evaluation of optical distortion is also presented.

Free Shear Layer

A two-dimensional shear layer was used as a test case in a series of numerical experiments. Sensitivities of mean and time-varying quantities to changes in time step size, fourth-order dissipation level, and grid refinement were determined. Additionally, the effect of the shear layer algebraic turbulence model was determined through comparison with similarity solutions and experimental data.

The computational domain for this case includes a 2-in. splitter plate embedded in a channel, with initial conditions specified as a discontinuous step at the channel centerline. The channel extends 30-in. downstream of the splitter plate trailing edge, and 5-in. above and below the plate. Inviscid walls were specified for 3-in. upstream of the splitter plate and for the channel walls. The inflow and outflow conditions were implemented using one-dimensional characteristic relations holding mass flow, total enthalpy, and flow angle fixed at the inlet, and fixing pressure at the exit plane. The boundary layers on the splitter plate and the shear layer were turbulent. Reynolds number based on the mean velocity of the streams and the length of the splitter plate was 6.7×10^5.

The results for three grid refinement levels are shown in Fig. 3 along with Görtler's similarity solution, where the velocity profiles are taken 10-in. downstream of the trailing edge of the plate. The solution becomes grid dependent for grids coarser than approximately 20 points across the layer. The Mach number ratio for this case was 0.2/0.8 and $\sigma = 20.7$. The eddy viscosity was observed to grow linearly in accordance with the Clauser formulation. In addition, numerical experiments to determine the dependence of p_{rms} on the level of fourth-order dissipation showed that a change in fourth-
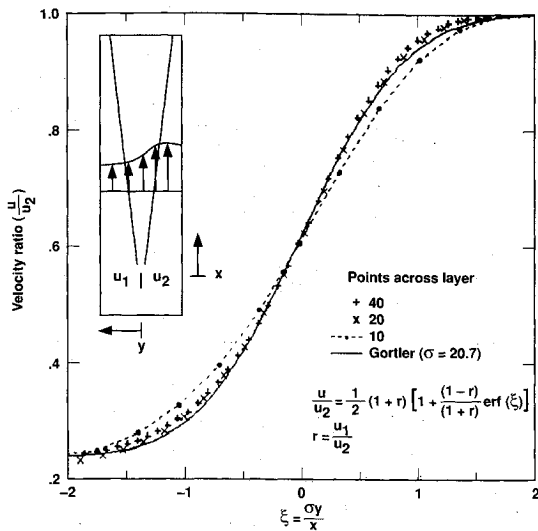
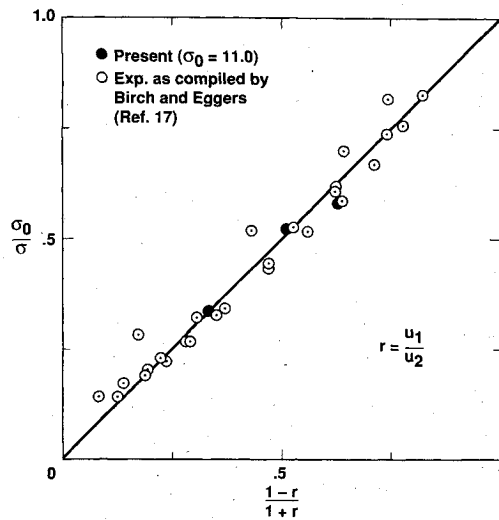**Fig. 3   Velocity profiles of differing grid resolution compared to similarity.**

Fig. 4   Variation of spread rate with velocity ratio.

Fig. 5   Two-dimensional cavity: a) topology and b) grids.
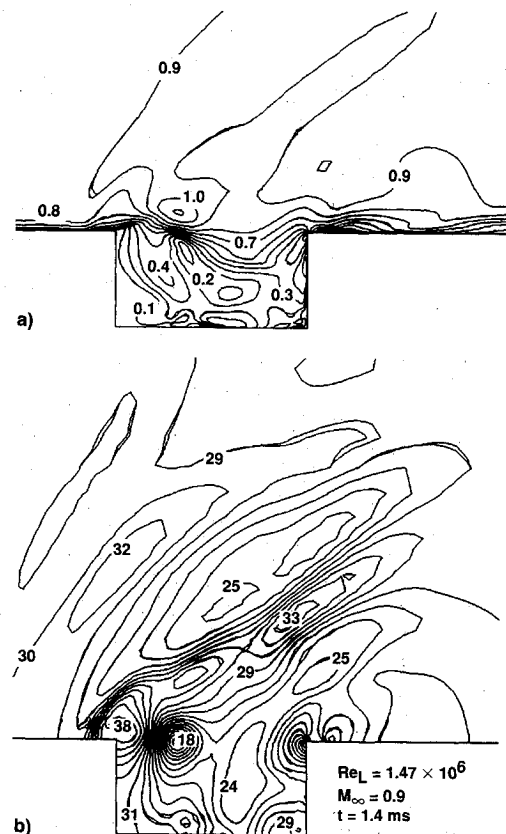
Fig. 6   Two-dimensional cavity: instantaneous a) Mach number and b) pressure (kPa) contours.

order smoothing from 0.01 to 0.05 caused a change of less than 1% in sound pressure level.

The velocity ratio across the SOFIA cavity shear layer will vary with streamwise location. Hence, comparison of the variation of spread rate with velocity ratio is shown in Fig. 4. The spreading parameter σ originates from the similarity solution shown in Fig. 3 and is inversely related to the spread rate, db/dx. The value of the σ when the velocity of one of the streams is zero is denoted σ_0. Three velocity ratios are shown for low Mach numbers with about 20 points maintained across the layer for all cases. The computed spreading rates are within the bounds of the experimental data.[17]

Two-Dimensional Cavity

The objective of this two-dimensional cavity case was to demonstrate the prediction of self-induced cavity resonance. Validation is provided by comparison against Rossiter's experimental data.[2] Sensitivity of the solution to topology, second-order dissipation, and turbulence model effects were determined.

The cavity geometry and grid topology is shown in Fig. 5, where the grid has been coarsened for clarity. The test conditions were set as

$$M_\infty = 0.9, \quad Re_L = 1.47 \times 10^6, \quad L = 8 \text{ in.}$$

The ratio of cavity length by depth (L/D) was 2 for this model. The inflow boundary was placed $7.5L$ upstream of the cavity
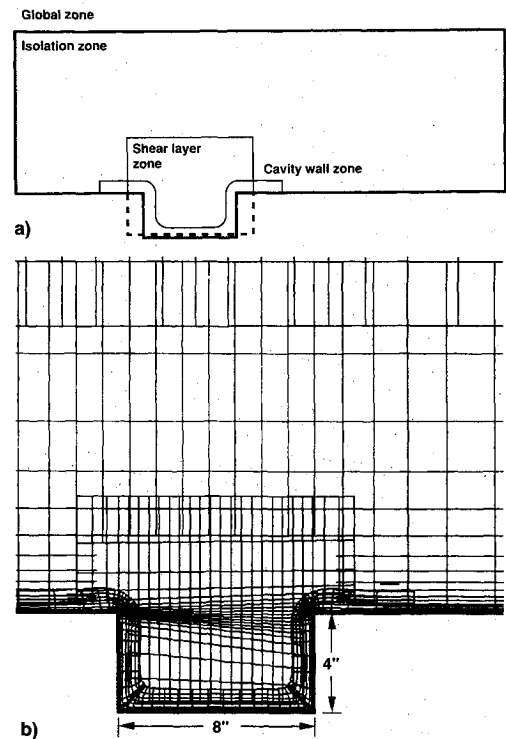
leading edge, the outflow boundary $4.5L$ downstream of the cavity trailing edge. The inflow and outflow conditions were specified as for the free shear layer cases, and an inviscid wall was placed $5L$ above the cavity.

Figure 6 depicts instantaneous Mach and pressure contours obtained during the computation in which the time step size was $\Delta t = 1.97 \ \mu s$. Inspection of the contours across zone
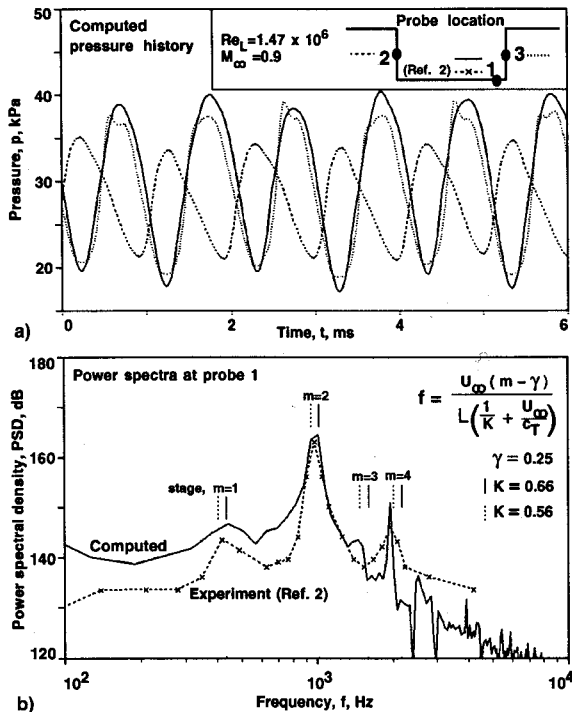
Fig. 7 Two-dimensional cavity: a) pressure history and b) power spectra comparison.

Fig. 8 Two-dimensional cavity: variation of mean and oscillatory pressures.

boundaries indicates that the interpolation process is well-behaved for this unsteady flow. The Mach contours show the prevalent oscillatory shear layer behavior. The pressure contours depict the feedback mechanism identified by Rossiter. Briefly, the cycle begins with the propagation of a wave from the aft wall of the cavity to the forward face. Wave reflection from the forward wall causes the shear layer to bow outwards, shedding vorticity. The deflected shear layer convects downstream and induces another cycle. The frequencies at which this feedback is reinforced is determined by the cavity recovery temperature and the shear layer convection speed.

The pressure histories and PSD along the cavity walls are depicted in Fig. 7, where comparison of Rossiter's data to present results indicates agreement in frequency at the peak magnitudes. Figure 7 also shows the frequencies predicted by Rossiter's formula[2] for two ratios of vortex by freestream speed K. Magnitudes are higher for the present case by about 2 dB; however for this experiment and other numerical work, this has been observed as an effect of cavity width W. In these studies,[2-9] the sound level was found to be inversely related to L/W; the cavity for Rossiter's experimental work was of $L/W = 2$. The PSD for this case was computed using 8192 time samples, no zero-padding, and a square window.

The solution was insensitive to variation of the second-order dissipation ε_2 in the range of 0.3–0.5. Additionally, in order to test a hypothesis of a limited domain of unsteadiness, an isolation zone was implemented as shown in Fig. 5. The flow outside the zones of interest was frozen, resulting in a decrease of the cavity sound pressure levels by 2%. A final comparison between experimental data and numerical results is provided in Fig. 8, where the variation of the mean and oscillatory pressures along the cavity walls is shown. Given the difference in spatial dimensions and turbulence modeling uncertainties, the trends appear reasonable for a flow of this complexity.

Clean Configuration

In order to provide a measure of validation, the geometry and flow conditions were chosen to replicate the wind tunnel tests:

$$M_\infty = 0.85, \quad Re_L = 4.2 \times 10^6$$

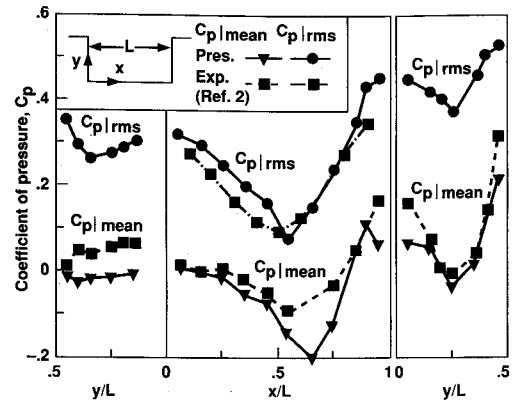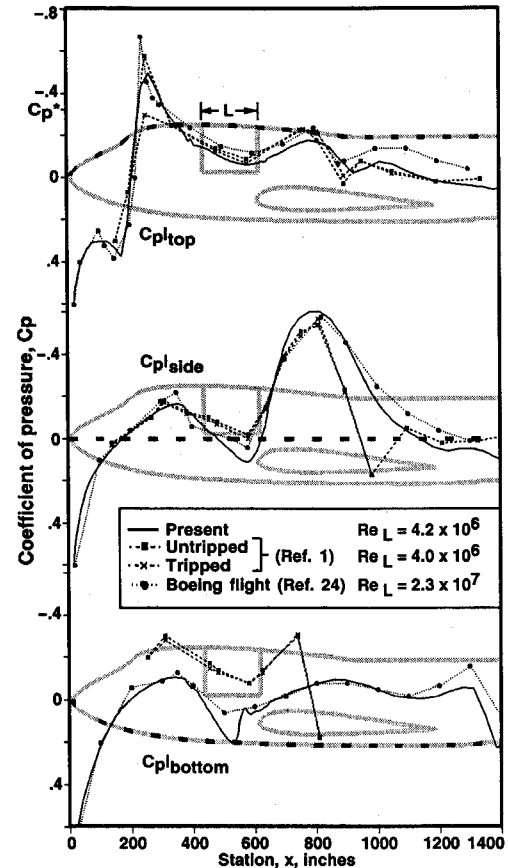$$L = 12.6 \text{ in.}, \quad \alpha = 2.5 \text{ deg}$$

Fig. 9 Clean configuration: pressure coefficient comparison.

Subsequent correction of the wind-tunnel data has resulted in the $Re_L = 4.0 \times 10^{-6}$, about 5% lower than above. The temperature difference from this correction causes the sound speed in these computations to be approximately 6% higher than experiment. Numerical results obtained for this 7% scale model are discussed below.

The wind-tunnel model without cavity was simulated in order to assess angle-of-attack errors owing to wind-tunnel wall effects. Figure 9 compares the present pressure coefficient profiles along the crest, side, and bottom of the model with wind-tunnel results[1] and flight data.[24] Experimental results are shown for both untripped and tripped cases; the latter case was used for all subsequent wind-tunnel testing. Although this comparison indicates that the influence of the tunnel wall was small near the cavity, pressures along the bottom of the model are shifted, possibly due to the effect of the tunnel floor. The residual, $|\delta p|_{max}$, dropped four orders of magnitude for this steady case.

Untreated Cavity: Configuration 25

The geometry shown in Fig. 10 was the initial cavity configuration tested in the wind tunnel. The objective of this simulation was the demonstration of self-excited cavity resonance in three dimensions. The flow conditions were the same as used above, the flowfield was initialized from the steady clean case. The stability-limited time step size used was $\Delta t = 3.53$ μs. This interval size corresponds to a $\nu \approx 1$ in the streamwise direction within the shear layer, and a $\nu_{max} \approx 500$.

Instantaneous Mach number contours in Fig. 11 show the flapping of the shear layer and the interpolation treatment. Sample pressure histories and PSD resulting from the wind tunnel and numerical efforts are shown in Fig. 12. The PSD was obtained using 2048 points, a Hanning window, and no zero-padding. The predicted frequencies of the resonant tones appear reasonable, and the computed dominant tone is within 3 dB of experiment. The magnitudes of the higher modes are much lower than found experimentally.

Estimation of the grid resolution required to maintain a propagating wave of proper magnitude can be deduced from the two-dimensional cavity and configuration 25 results. First, wavelength can be estimated by assuming the wave to be harmonic at a given frequency and traveling at the local speed of sound. Next, it is noted that frequencies of 2 kHz were resolved well in the two-dimensional case, in which the grid resolution was such that about 40 points supported the wave. From the configuration 25 results, it is seen that only the 700 Hz peak is well-resolved, which again gives approximately 40 points across the wave for this coarser grid. Although numerical damping of the higher frequencies can be expected,
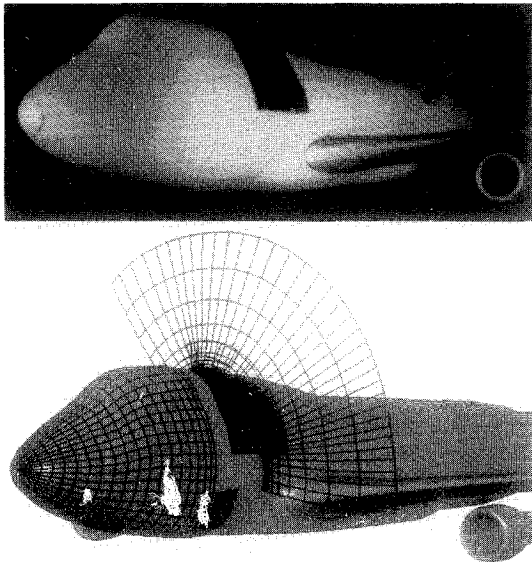

Fig. 10   Configuration 25: wind tunnel and numerical models.

$Re_L = 4.2 \times 10^6$
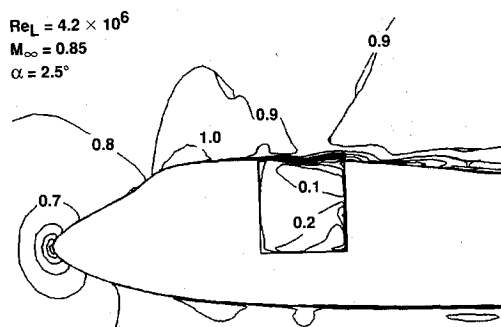$M_\infty = 0.85$
$\alpha = 2.5°$

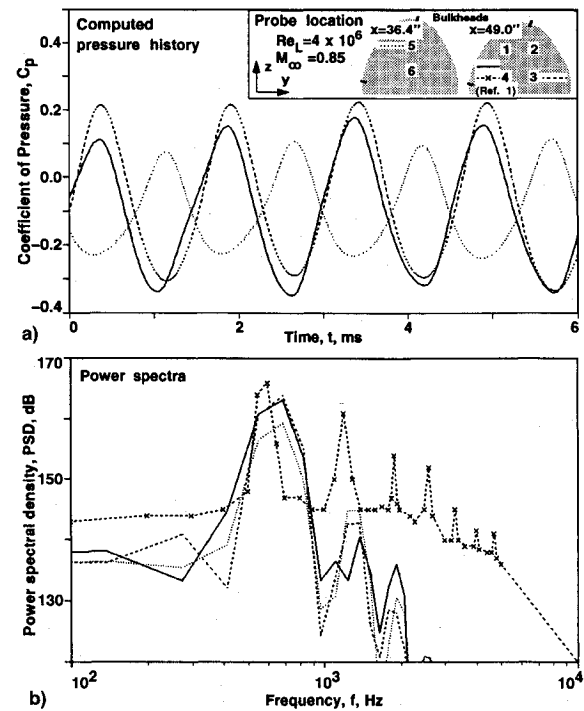Fig. 11   Configuration 25: Mach number contours at $y = 0$.

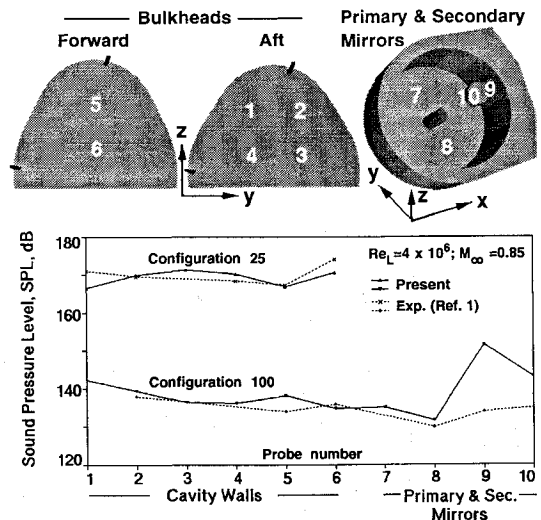Fig. 12   Configuration 25: a) pressure histories and b) power spectra.

Fig. 13   Comparison of sound pressure levels.

most of the energy is contained in the lowest frequency mode, as can be seen in the SPL comparison of Fig. 13. The SPL for the resonating and quieted geometries obtained numerically are in reasonable agreement with experiment. Improvement may be obtained using higher-order spatial approximations or by grid refinement.

Treated Cavity: Configuration 100

In 1990, an investigation of SOFIA cavity quieting treatments was performed in the NASA/ARC 14 × 14-ft wind tunnel.[1] Of the many geometries tested, configuration 100 resulted in the lowest sound production levels. This simulation was implemented in order to determine if the same level of quieting would be predicted numerically as was found experimentally. Previous investigations[12] of cavity noise suppression have shown aft ramp treatments to be effective, possibly by allowing a stable shear layer reattachment site. For the SOFIA experiment, this type of geometry treatment was found to be quieter than the untreated configuration 25 case by over 30 dB. Figure 13 shows that the proper trend is computed. The flow conditions were again initialized from the clean case.
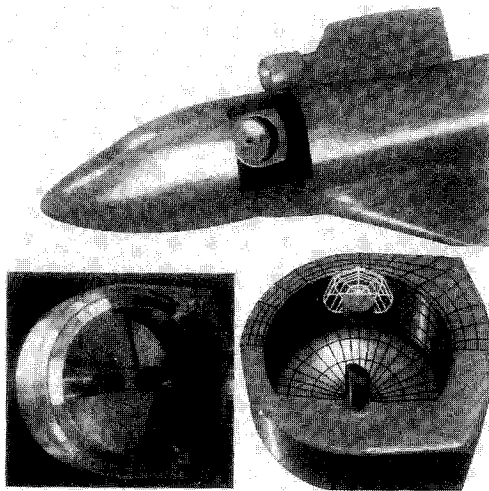
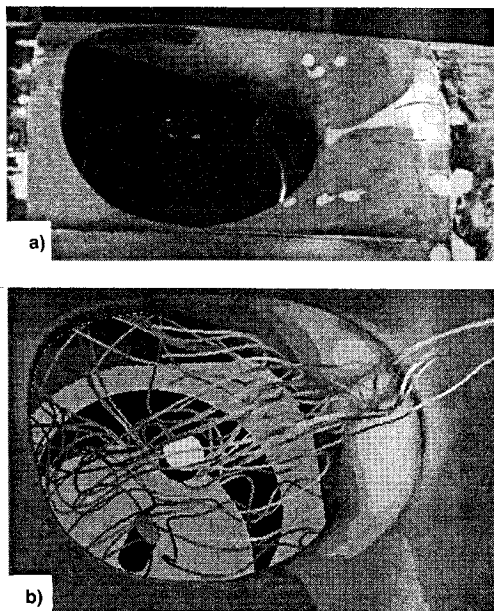Fig. 14   Telescope location and grids.

Fig. 15   Configuration 100: treated aperture a) wind-tunnel model and b) numerical model with instantaneous streamlines.

The stability-limited time step size used was $\Delta t = 7.06$ μs. The PSD was obtained using 4096 points, a Hanning window, and no zero-padding.

Figure 14 shows the position of the telescope in the aircraft and the coarsened telescope grids. Figure 15 depicts the aft ramp treatment modeled for this case along with computed particle traces, and Fig. 16 shows the topology used in the cavity region, where again the grids have been coarsened for clarity. Figure 17 compares time-mean experimental and computational shear layer Mach profiles. The vertical scale of the profiles is twice that shown in the contour plot for clarity. Note that the experimental profiles were obtained using a rake, which is sensitive only to u, the x component of velocity. The computed discrepancy between $|u|/c$ and $|V|/c$ is approximately 0.05 at the lower speed end of the profile. Figure 17 indicates reasonable agreement for growth rates, though the profile shapes become quite different as the shear layer approaches the ramp. This discrepancy may be in part due to probe position uncertainty and geometry modifications to allow for the probe mechanism. These modifications included removal of the telescope assembly and cutting a streamwise slot in the ramp. Time averaging of velocities was performed over 1000 time steps and profiles were insensitive to segment length.
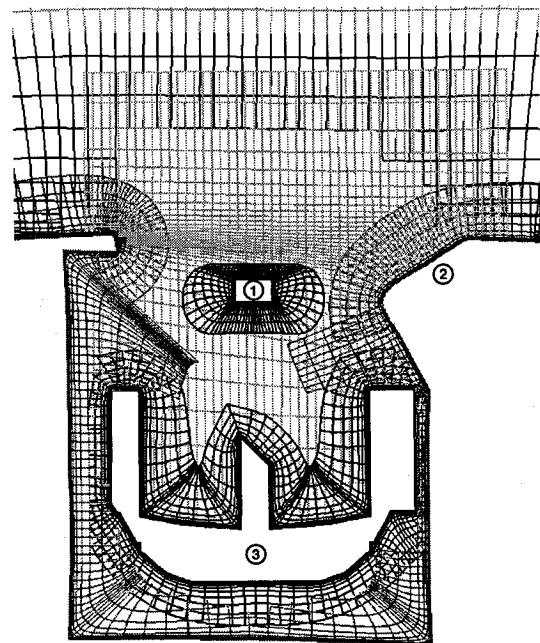
① Secondary mirror
② Aft ramp
③ Primary and tertiary mirror assembly

Fig. 16   Configuration 100: cavity region topology.
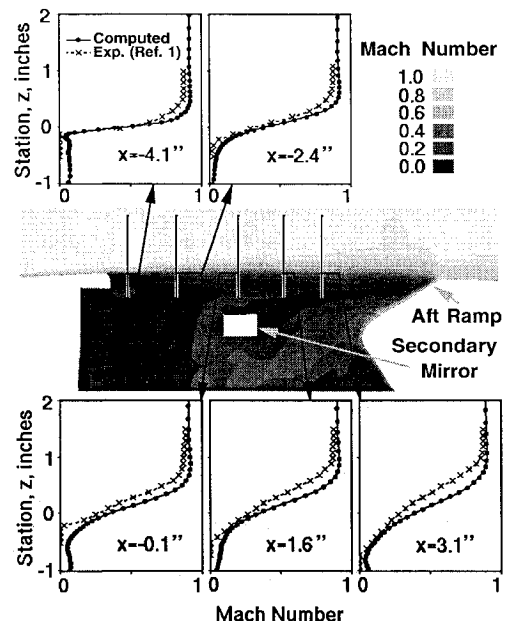

Fig. 17   Configuration 100: mean Mach number profiles.

Figure 18 shows the pressure history and resultant PSD on the cavity walls. Although the peak spectra levels are in agreement, the spectra levels can again be seen to drop more rapidly with frequency for the numerical results as compared to experiment. The pressures on the primary mirror show lower high frequency content with the peak at 1800 Hz not resolved. The pressure variations on the secondary mirror show a low frequency component which was not found experimentally. This discrepancy is manifested as the SPL difference seen in Fig. 13.

Aero-Optics

Application of the geometric optics code to two preliminary test cases was undertaken to determine the sensitivity of the code to the nonunique partitioning, or tesselation of the hex-
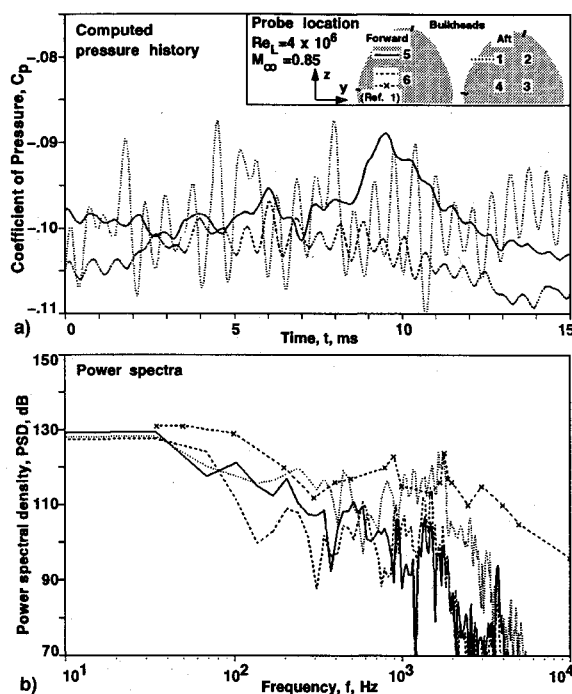
Fig. 18 Configuration 100: a) pressure history and b) power spectra on cavity wall.
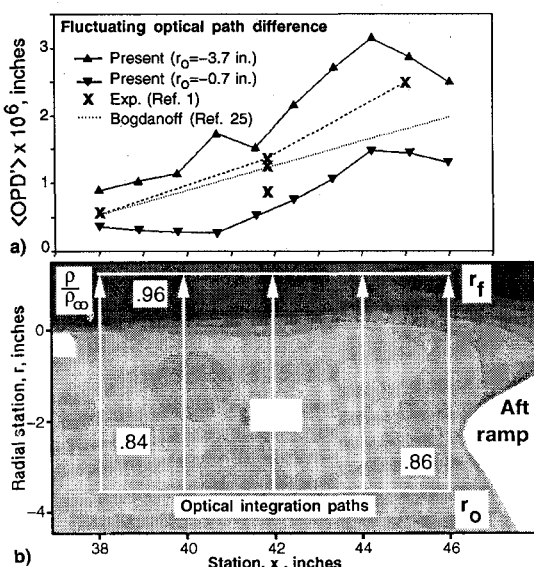

Fig. 19 Comparison of: a) wavefront distortion and b) optical refraction model.

ahedrons. The parallel emergence of the rays after propagation through a plate of high index of refraction implies that the results are relatively insensitive to the method of tesselation.

The optics code was applied to the density field obtained from configuration 100 at the crossflow center of the aperture, shown schematically in Fig. 19b. Ten rays were propagated through 110 density fields in time intervals of $\Delta t = 70.6 \mu s$, sufficient for several shear layer perturbation cycles to occur. Computed fluctuating optical path differences, $\langle OPD' \rangle$, are compared to experiment[1] and previous analysis[25] in Fig. 19a. Two computed results are shown, one for the optical integration paths originating immediately below the shear layer ($r_0 = -0.7$ in.), and the other for rays initialized below the secondary mirror ($r_0 = -3.7$ in.). All computed integration paths terminate at $r_f = 2.3$ in. Shear layer aerodynamic measurements of Rose and Cooley[1] were used to determine distortion for the experimental data shown in Fig. 19, while the

analytic result assumes an index-matched shear layer with a sinusoidal n profile.

Figure 19a shows that the distortion model applied through the shear layer alone ($r_0 = -0.7$ in.) underpredicts the data determined analytically and experimentally. However, the computed trend is generally consistent with the data. Comparison of the computed results for $r_0 = -0.7$ in. and $r_0 = -3.7$ in. shows an increment in $\langle OPD' \rangle$. This distortion increment appears to be caused by a jet of fluid resulting from the impingement of the shear layer on the aft ramp.

Conclusions

The work presented here is the initial effort towards development of a design and analysis tool for use throughout the SOFIA project life. Thus far, this investigation has demonstrated that self-induced cavity resonance can be accurately captured for complex two- and three-dimensional geometries modeled using an overset mesh topology while maintaining efficiency through isolation of the unsteady flow region. The computed performance of a cavity quieting treatment was generally in good agreement with experimental data. The cost of each of the unsteady three-dimensional computations was approximately 80 Cray Y-MP hours.

Predicted shear layer profiles and resonant behavior are consistent with previous analytic and experimental work. Generally, sound pressure levels agree to within 4%, and improvements in the energy distribution in frequency may be attained by use of higher-order spatial approximations, or more simply by grid refinement. Although topology treatment has allowed the simple specification of turbulent wall and shear layer regions, a higher-order turbulence model may offer increased accuracy.

The geometric aero-optical model shows proper trends, but the distortion magnitude is underpredicted. The goal of providing detailed aero-optical design information requires further investigation to achieve improved wavefront distortion results.

References

[1]Rose, W. C., and Cooley, J. M., "SOFIA Wind Tunnel Data Analysis and Implications for the Full-Scale Aircraft," Rose Engineering and Research, Incline Village, NV, Dec. 1990.

[2]Rossiter, J. E., "Wind-Tunnel Experiments on the Flow over Rectangular Cavities at Subsonic and Transonic Speeds," Royal Aircraft Establishment Rept. and Memoranda 3438, UK, Oct. 1964.

[3]Neary, M. D., "Time Dependent Self-Sustaining Oscillations of Cavity Flow," AIAA Paper 87-0142, Jan. 1987.

[4]Hankey, W. L., and Shang, J. S., "Analysis of Pressure Oscillations in an Open Cavity," AIAA Journal, Vol. 18, Aug. 1980, pp. 892–898.

[5]Venkatapathy, E., Lombard, C. K., and Nagaraj, N., "Numerical Simulation of Compressible Flow Around Complex Two-Dimensional Cavities," AIAA Paper 87-0116, Jan. 1987.

[6]Om, D., "Navier-Stokes Simulation for Flow Past an Open Cavity," Journal of Aircraft, Vol. 25, No. 9, 1988, pp. 842–848.

[7]Dougherty, N. S., Holt, J. B., Nesman, T. E., and Farr, R. A., "Time-Accurate Navier-Stokes Computations of Self-Excited Two-Dimensional Unsteady Cavity Flows," AIAA Paper 90-0691, Jan. 1990.

[8]Suhs, N. E.,"Computations of Three-Dimensional Cavity Flow at Subsonic and Supersonic Mach Numbers," AIAA Paper 87–1208, June 1987.

[9]Rizzetta, D. P., "Numerical Simulation of Supersonic Flow over a Three-Dimensional Cavity," AIAA Journal, Vol. 26, July 1988, pp. 799–807.

[10]Baysal, O., and Stallings, R. L., Jr., "Computational and Experimental Investigation of Cavity Flowfields," AIAA Paper 87-0114, Jan. 1987.

[11]Löhner, R., "Three-Dimensional Fluid-Structure Interaction Using a Finite Element Solver and Adaptive Remeshing," Computing Systems in Engineering, Vol. 1, Nos. 2–4, 1990, pp. 257–272.

[12]Komerath, N. M., Ahuja, K. K., and Chambers, F. W., "Prediction and Measurement of Flows over Cavities—A Survey," AIAA Paper 87-0166, Jan. 1987.

[13]Buning, P. G., and Chan, W. M., "OVERFLOW/F3D User's Manual, Version 1.5," NASA/ARC, Nov. 1990.

[14]Benek, J. A., Buning, P. G., and Steger, J. L., "A 3-D Chimera Grid Embedding Technique," AIAA Paper 85-1523, July 1985.

[15]Pulliam, T. H., and Chaussee, D. S., "A Diagonal Form of an Implicit Approximate-Factorization Algorithm," Journal of Computational Physics, Vol. 39, Feb. 1981, pp. 347–363.

[16]Baldwin, B. S., and Lomax, H., "Thin-Layer Approximation and Algebraic Model for Separated Turbulent Flows," AIAA Paper 78-257, Jan. 1978.

[17]Birch, S. F., and Eggers, J. M., "A Critical Review of the Experimental Data for Developed Free Turbulent Shear Layers," Free Turbulent Shear Flows, NASA SP-321, July 1972.

[18]Atwood, C. A., and Vogel, J. M., "Surface Grid Generation for Flowfield Applications Using B-Spline Surfaces," AIAA Paper 89-2177, Aug. 1989.

[19]Merriam, M. L., and Barth, T. J., "3-D CFD in a Day: The Laser Digitizer Project," AIAA Paper 91-1654, June 1991.

[20]Vaillancourt, K., private communication, NASA/ARC, Moffett Field, CA.

[21]Steinbrenner, J. P., Chawner, J. R., and Fouts, C. L., "A Structured Approach to Interactive Multiple Block Grid Generation," AGARD FDP Specialists Meeting on Mesh Generation for Complex Three-Dimensional Configurations, Loen, Norway, May 1989.

[22]Parks, S. J., Buning, P. G., Steger, J. L., and Chan, W. M., "Collar Grids for Intersecting Geometric Components Within the Chimera Overlapped Grid Scheme," AIAA Paper 91-1587, June 1991.

[23]Chan, W. M., and Steger, J. L., "A Generalized Scheme for Three-Dimensional Hyperbolic Grid Generation," AIAA Paper 91-1588, June 1991.

[24]Haslund, R. L., "SOFIA Viewport Configuration Wind Tunnel Test Report," Boeing Aerospace and Electronics Sensors Technology, Seattle, WA, Oct. 1988.

[25]Bogdanoff, D. W., "The Optical Quality of Shear Layers: Prediction and Improvement Thereof," AIAA Journal, Vol. 22, Jan. 1984, pp. 58–64.